J Neuropathol Exp Neurol
Vol. 73, No. 4
April 2014
pp. 345–361

ORIGINAL ARTICLE

Repetitive Mild Traumatic Brain Injury Causes Optic Nerve and Retinal Damage in a Mouse Model

Radouil Tzekov, MD, PhD, Alexandra Quezada, Megan Gautier, BA, Davida Biggins, Candice Frances, Benoit Mouzon, PhD, Jeff Jamison, PhD, Michael Mullan, MD, PhD, and Fiona Crawford, PhD

Abstract

There is increasing evidence that long-lasting morphologic and functional consequences can be present in the human visual system after repetitive mild traumatic brain injury (r-mTBI). The exact location and extent of the damage in this condition are not well understood. Using a recently developed mouse model of r-mTBI, we assessed the effects on the retina and optic nerve using histology and immunohistochemistry, electroretinography (ERG), and spectral-domain optical coherence tomography (SD-OCT) at 10 and 13 weeks after injury. Control mice received repetitive anesthesia alone (r-sham). We observed decreased optic nerve diameters and increased cellularity and areas of demyelination in optic nerves in r-mTBI versus r-sham mice. There were concomitant areas of decreased cellularity in the retinal ganglion cell layer and approximately 67% decrease in brain-specific homeobox/POU domain protein 3A–positive retinal ganglion cells in retinal flat mounts. Furthermore, SD-OCT demonstrated a detectable thinning of the inner retina; ERG demonstrated a decrease in the amplitude of the photopic negative response without any change in a- or b-wave amplitude or timing. Thus, the ERG and SD-OCT data correlated well with changes detected by morphometric, histologic, and immunohistochemical methods, thereby supporting the use of these noninvasive methods in the assessment of visual function and morphology in clinical cases of mTBI.

Key Words: Electroretinography, Ganglion cells, Mild traumatic brain injury, Optic nerve, Retina, Spectral-domain optical coherence tomography.

INTRODUCTION

Traumatic brain injury (TBI) is a major cause of death and disability, with an estimated worldwide incidence of about 10 million cases per year (1). The annual incidence in the United States alone is approximately 1.7 million (2), with estimated medical costs of $56.5 billion in 2000 (3). These figures are likely an underestimate of the true incidence of injury and cost because cases of TBI are often unreported.

Traumatic brain injury severity is commonly described as mild, moderate, or severe based on a number of factors such as the duration of loss of consciousness and/or coma rating scale or score, posttraumatic amnesia, and brain imaging results (4). Concussion, or mild TBI (mTBI), is the most common form of TBI, accounting for up to 75% of all brain injuries occurring annually in the United States (2).

Ocular and vision damage has been reported previously as a consequence of TBI, including mTBI, as part of the postconcussion syndrome (5–8). Thus, symptoms of photosensitivity, blurred vision, double vision, decreased visual acuity, and visual field defects are often described. However, the mechanisms leading to these short- or long-term negative impacts on visual function and abilities are poorly understood.

Recently, changes in surrogate measures of visual function and ocular structures have been reported in rodent studies using a single blast injury focused on the head (9). The authors found a decrease in retinal nerve fiber layer (RNFL) thickness and a decrease in pattern electroretinography (ERG) 3 to 4 months after injury, which correlated with punctate regions of reduced cellularity in the ganglion cell layer and damage to the optic nerve. While relevant for some forms of human TBI, in particular certain military exposures, blast models relate to injuries that occur relatively rarely within the spectrum of human TBI.

We have recently developed a mouse model to enable characterization of the consequences of repetitive mild TBI (r-mTBI) in closed head injury. Extensive neurobehavioral and neuropathologic analyses of this model have demonstrated the deleterious effects of r-mTBI on brain morphology and cognitive function (10–12). Whether r-mTBI has any significant quantifiable negative consequences for the visual system is unclear. The purpose of the present study was to use this novel model to characterize the effects of r-mTBI on the mouse visual system.

MATERIALS AND METHODS

Animal Handling

All procedures were carried out according to the Association for Research in Vision and Ophthalmology statement for the Use of Animals in Ophthalmic and Vision Research,

From the Roskamp Institute, Sarasota (RT, AQ, MG, DB, CF, BM, MM, FC); and University of South Florida, Tampa (RT), Florida; Ophthy-DS, Inc., Kalamazoo, Michigan (JJ); and James A. Haley Veteran's Administration, Tampa, Florida (RT, BM, MM, FC).

Send correspondence and reprint requests to: Radouil Tzekov, MD, PhD, The Roskamp Institute, 2040 Whitfield Ave, Sarasota, FL 34243; E-mail: rtzekov@roskampinstitute.net

This work was supported by Department of Defense award W81XWH-10-1-0759 (to Fiona Crawford) and by the Roskamp Foundation.

Supplemental digital content is available for this article. Direct URL citations appear in the printed text and are provided in the HTML and PDF versions of this article on the journal's Web site (www.jneuropath.com).

the Association for Assessment and Accreditation of Laboratory Animal Care and were approved by the local Institutional Animal Care and Use Committee.

Adult C57BL/6 male mice (aged 8–10 weeks) were randomly assigned to either r-mTBI or repetitive sham (r-sham; anesthesia only) groups. Five consecutive hits with an interconcussion interval of 48 hours were applied, according to an established method that causes no skull fractures, hemorrhages, or cerebral contusions (10). Briefly, mice were anesthetized with isoflurane and placed on a heating pad. The injury was triggered using an electromagnetic controlled impact device with a 5-mm blunt metal impactor tip (Impact One Stereotaxic Impactor, Leica Biosystems, Buffalo Grove, IL) at a strike velocity of 5 m per second, strike depth of 1.0 mm, and dwell time of 200 milliseconds. The location of the impact on the skull was central, equally distant from both eyes (Figure 2 in Mouzon et al [10]). Sham mice received anesthesia of equal duration to the injured mice and at the same intervals.

Injury Groups and Schedule

Cohorts of mice were killed at 10 and 13 weeks after r-mTBI (n = 12) or r-sham (n = 12), and the eyes and optic nerves were examined histologically. A subset of the mice was examined at 10 weeks after the last injury by spectral-domain optical coherence tomography (SD-OCT) and ERG.

In addition, naive C57BL/6 mice (both male and female) aged 6 to 9 months (n = 7) were obtained from Jackson Laboratories (Bar Harbor, ME) and were used as a reference group for SD-OCT and histology.

Retinal and Optic Nerve Histology

The animals were deeply anesthetized with isoflurane. They were then intracardially perfused by gravity drip with a heparinized PBS solution and 4% paraformaldehyde for 3 minutes. The eyes and optic nerves were extracted separately by cutting the optic nerve approximately 0.5 mm from the posterior pole of the eyeball. Low-temperature cautery was used to mark the 12-o'clock position on each cornea; care was taken to ensure that the mark remained visible throughout the processing. Both eye and optic nerve specimens were fixed in 10% neutral buffered formalin (BBC Biochemical, Everett, WA) at 4°C for 24 hours and then transferred into 80% ethanol for long-term storage. Samples were processed for paraffin embedding using a standard protocol and embedded in paraffin in such a way as to ensure a cut through the vertical meridian of the eyeball and a longitudinal cut through the optic nerve. Paraffin blocks were sectioned at a thickness of 4 μm with a Leica RM2235 microtome (Leica Microsystems Inc., Buffalo Grove, IL) and mounted on positively charged glass slides (Erie Scientific, Portsmouth, NH).

Hematoxylin and eosin (H&E) staining was applied to the optic nerves and eye cross sections. In addition, Luxol fast blue (LFB) staining with cresyl violet (CV) as a counterstain was applied to the optic nerve cross sections.

Estimating Cellularity in the Retinal Ganglion Cell Layer

Cellularity in the retinal ganglion cell (RGC) layer was determined by image analysis in 3 adjacent areas in the upper and 3 adjacent areas in the lower retina on H&E-stained retinal cross sections cut through the vertical meridian from mice at 10 weeks after injury (n = 4, r-sham; n = 4, r-mTBI). Three adjacent image fields, each corresponding in size to 40× microscopic field, were outlined starting at approximately 600 μm from the center of the optic disc in the upper and in the lower retina. The purpose of this selection was to avoid areas of multilayer cellular distribution that are typically present in the RGC layer in mice and other mammals. All cell nuclei in the RGC layer were counted using image processing software (ImageJ, version 1.48; National Institutes of Health, Bethesda, MD [13]). Briefly, images were converted to 8-bit format and then adjusted for contrast, brightness, and threshold. Larger areas, where the cells were perceived as fused, were subdivided using a watershed procedure in ImageJ. The cells in each of the 3 adjacent areas were counted individually by enclosing the region of interest with the selection tool and using the Analyze Particles method available as part of ImageJ. Results from this counting method correlated well ($r = 0.95$) with the estimates obtained with manual counting of 5 images.

Flat Mount Preparation and RGC Counting

Whole-mount retinal preparation of mice at 13 weeks after injury (n = 3, r-sham; n = 6, r-mTBI) was carried out using a method similar to that described by Salinas-Navarro et al (14), with slight modifications. Briefly, mice were deeply anesthetized, and the vertical orientation of the eye was marked by low-temperature cautery. On dissection of the eyeball, the rectus muscle insertion into the superior part of the eye and the nasal caruncle were used as additional landmarks. Both retinas were dissected and prepared as flattened whole mounts by making 4 radial cuts (the deepest in the superior pole), postfixed for an additional 1 hour, and then transferred into a 2-mL vial.

Immunofluorescence staining with an antibody against brain-specific homeobox/POU domain protein 3A (Brn-3a) was performed similar to the methods described in Galindo-Romero et al (15). Briefly, retinas were permeated in PBS 0.5% Triton X-100 by freezing them for 15 minutes at −70°C; they were then rinsed in fresh PBS 0.5% Triton and incubated overnight at 4°C with a primary goat anti-BRN3A (C-20) antibody (Santa Cruz Biotechnology Inc., Santa Cruz, CA) diluted 1:100 in blocking buffer (PBS, 2% bovine serum albumin, 2% Triton). Retinas were then washed 3 times in PBS and incubated for 2 hours at room temperature with the secondary antibody (Alexa Fluor 594-AffiniPure Rabbit Anti-Goat IgG; Jackson ImmunoResearch Laboratories Inc., West Grove, PA) diluted 1:500 in blocking buffer. Finally, retinas were thoroughly washed in PBS and mounted vitreal side up on slides and covered with antifading solution.

Counting of Ganglion Cells

For each whole mount, a series of nonoverlapping images were taken with a motorized stage (ProScan; Prior Scientific Inc., Rockland, MA) and an XM10 camera attached to an Olympus BX63 microscope (Olympus America, Center Valley, PA) using a Texas red filter cube. Because of the difference in focal plane across the retinal preparation, focus stacking was performed to ensure that RGC nuclei were always

in focus. The stacked mosaics of images were then exported and subsequently combined into 1 frame using the maximal intensity projection method in ImageJ. After background adjustment, the images were converted to 8-bit format and then adjusted for contrast, brightness, and threshold. Larger areas where the cells were perceived as fused were subdivided using a watershed procedure. The RGC nuclei were counted with an automated counting algorithm in ImageJ within the cell nucleus size range of 10 to 300 mm^2, similar to one used in published literature (15). The coordinates of all cells were then exported in MS Excel software (Microsoft Inc., Redmond, WA), and a preliminary map was constructed based on a grid line distance of 150 μm (grid cell area, 0.0225 mm^2). A final filled contour plot map was then generated in Sigma Plot 8.0 (Systat Software, Inc., San Jose, CA). To estimate the differences in the magnitude of cell loss in the center versus periphery, 4 concentric circles (with increasing radius steps of 600 μm) were drawn on the thresholded image and the number of Brn-3a–positive cells was determined within the retinal area of each circular region.

Optic Nerve Morphometry

After death and removal of the eyeballs, optic nerves at 13 weeks after injury (n = 5, r-sham; n = 6, r-mTBI) were carefully separated from the rest of the tissue and placed on a glass slide above a dark background. All optic nerve preparations were imaged with a calibrated camera (OQCLR3C; QImaging, Surrey, British Columbia, Canada) attached to an Olympus SZX10 stereomicroscope (Olympus America). Images were saved in TIFF format and analyzed in ImageJ. The length of the optic nerves was determined by drawing a line through the estimated center part of each nerve from the chiasm to the end of the sample. The thickness was measured by drawing perpendicular lines to the main line at every 500 μm along the length of the nerve. After completion of the imaging procedure, the optic nerves were processed for paraffin embedding as described below.

Estimating Cellularity in the Optic Nerve

Cellularity in the optic nerve tissue was estimated in the paraffin-embedded, H&E-stained longitudinal sections of nerves from naive, r-sham, and r-mTBI mice at 10 weeks after injury (n = 6, naive; n = 5, r-sham; n = 3, r-mTBI). Optic nerve cell nuclei were counted using ImageJ software. First, images were converted into 8-bit gray-scale images, and the background was subtracted using the software procedure available. Brightness and contrast were manually adjusted. The image was then converted into a binary format with a manually optimized threshold. The watershed subroutine was used to separate nuclei with a common border. Starting from the periocular end, rectangular areas equivalent in size to 40× microscopic field were generated along the entire length of the optic nerve such that they did not overlap but incorporated as much surface area of the optic nerve as possible. Cells were counted and measured using the particle analyzer included in ImageJ. The average minimum, maximum, perimeter, circularity, percent area, roundness, solidity, and count for each box were recorded. For boxes that encompassed areas outside the optic nerve boundaries, the region of interest including only the optic nerve tissue within the rectangular area was measured and recorded with the data. Cell density (in cells per square millimeter) was calculated for each area based on cell nuclei count and the area of region of interest.

Immunohistochemistry

Optic nerve specimens were obtained, processed, and mounted on slides as described above. Sections were deparaffinized in xylene and rehydrated in a decreasing gradient of ethanols. The sections were then rinsed in water and subsequently incubated at room temperature in a solution of endogenous peroxidase blocking solution, containing 0.3% H_2O_2 diluted in PBS (0.1 mol/L, pH 7.4) for 30 minutes. After rinsing, sections were treated with target retrieval solution for 8 minutes in a microwave for antigen retrieval. Further incubation with either protein block "serum-free" solution (Dako, Carpinteria, CA) or mouse immunoglobulin G blocking reagent (mouse on mouse [MOM] Kit; Vector Laboratories, Burlingame, CA) (depending on antibody used) was performed for a period of 1 hour in a humid chamber at room temperature.

Sections were stained in batches with primary antibodies raised against glial fibrillary acidic protein (GFAP) (rabbit anti-GFAP, 1:10,000; Dako) for astrocytosis and ionized calcium-binding adaptor molecule 1 (Iba-1) for microglia. As a negative control, 1 section was incubated with all reagents except the primary antibody. Tissue sections stained with Iba-1 were subjected to antigen retrieval with modified citrate buffer (Dako) under pressure. Endogenous peroxidase activity was quenched with a 15-minute H_2O_2 treatment (3% in water). Each section was rinsed and incubated with the appropriate blocking buffer (ABC Elite kit; Vector Laboratories) for 30 minutes before applying the appropriate primary antibody overnight at 4°C. The diluted biotinylated secondary antibody from the ABC Elite Kit was then applied on each glass slide. Antibodies were detected using the avidin-peroxidase complex, and labeling was revealed after incubating the sections in 3,3′-diaminobenzidine (DAB) peroxidase solution (0.05% DAB–0.015% H_2O_2 in 0.01 mol/L PBS, pH 7.2) for 6 to 7 minutes.

Optical Coherence Tomography

Spectral-domain OCT was performed in a subset of animals (r-sham, n = 3; r-mTBI, n = 6) at 10 weeks after injury. Animals were anesthetized with a portable isoflurane inhalation system (Summit Medical Equipment Company, Bend, OR) after initial induction in a chamber with 2% (vol) isoflurane at 2 L/minute oxygen flow. Their pupils were dilated with 1% tropicamide (Alcon Laboratories, Ft. Worth, TX) and 5% phenylephrine hydrochloride (EyePhrine, Eye Supply, Tampa, FL), and the animals were placed on a custom-designed platform in front of the SD-OCT instrument. Anesthesia was maintained by applying 1.5% to 1.8% isoflurane via a nose cone at 0.8 L/minute oxygen flow throughout the imaging session. Heidelberg Spectralis HRA + OCT system (Heidelberg Engineering, Vista, CA) was used, without any modification of the optical path. B-scan images of the retina were acquired in 2 modes: a circular ring scan ($r = \sim 1.4$ mm) and a starlike pattern of 4 line scans—both centered on the optic nerve head. Eye motion artifacts were eliminated by in-system eye tracking, and at least 25 frames were averaged per B-scan to increase the signal-to-noise ratio.

To obtain measurements from the B-scan, layer lines automatically defined by Heidelberg software were manually adjusted. Both total retinal thickness (TRT) and inner retinal thickness (IRT) were measured. Total retinal thickness was measured from the vitreo-retinal surface to the retinal pigment epithelium/Bruch membrane complex as delineated by the segmentation algorithm used in the SD-OCT software (Spectralis-OCT Viewing Module, Heidelberg Eye Explorer, Heidelberg Engineering). Inner retinal thickness was measured between the internal limiting membrane and the outer nuclear layer, a feature clearly delineated on an OCT scan of the mouse retina (16).

Data from the circular ring scan for both thickness measurements were analyzed in 2 ways. First, an average value was calculated for each of 4 quadrants, that is, superior (S), temporal (T), inferior (I), and nasal (N). Furthermore, to examine the spatial variability of the retinal thickness in more detail, each quadrant segment was subdivided into 2 sectors. Thus, a total of 8 segment sectors were analyzed, and the average retinal thickness value was calculated for each sector (Fig. 1A). Retinal thickness (both total retina and inner retina) from the starlike pattern of line scans was analyzed at 4 locations for each line scan, that is, at both ends of the line scan and at 2 points located

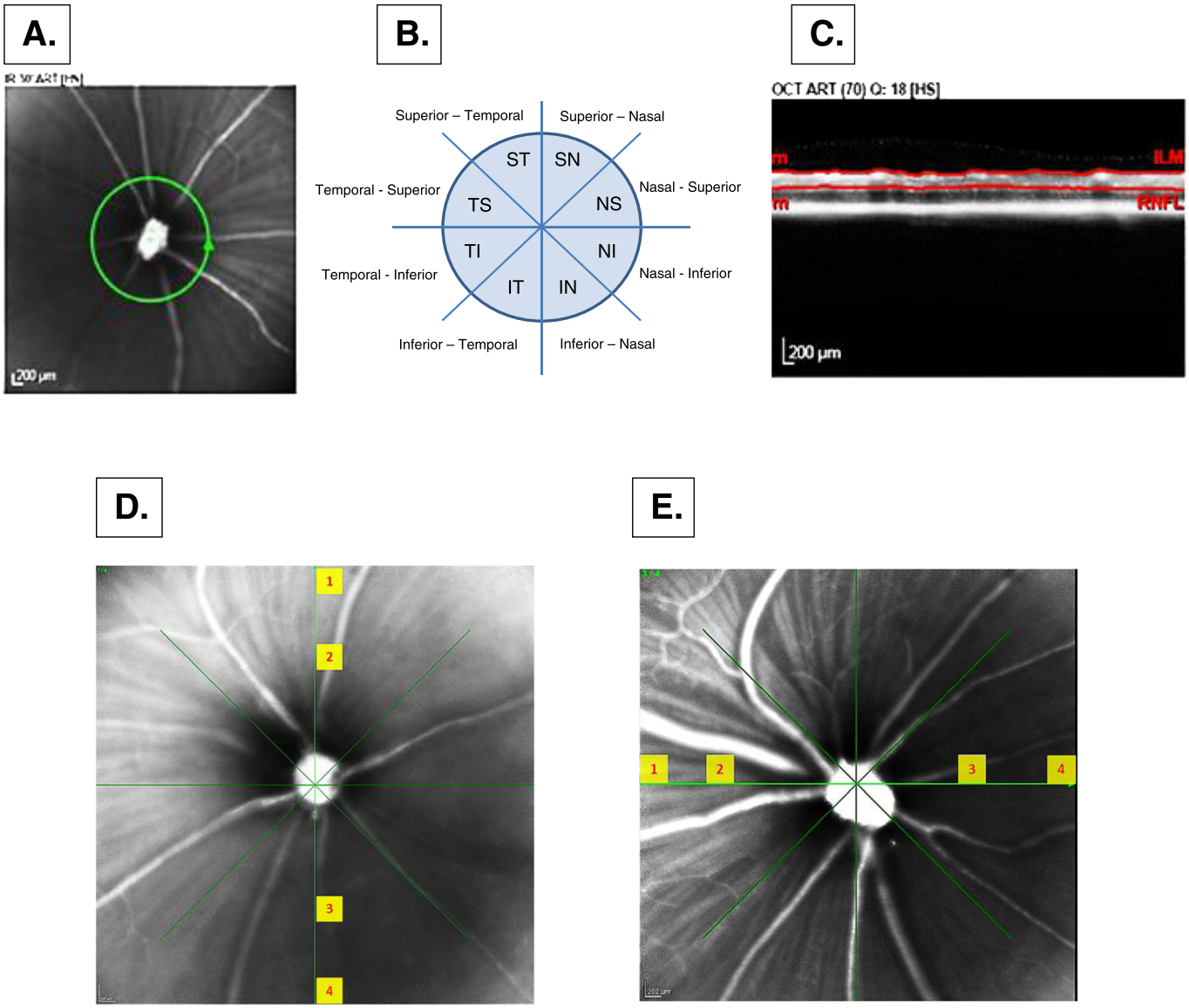

FIGURE 1. Spectral-domain optical coherence tomography image acquisition and analysis. **(A)** Position of the circular scan on the retina. **(B)** Schematic representation of the subdivision of the circular scan in 8 sectors. **(C)** Representative image of an unwrapped circular B-scan with segmentation lines indicating the inner limiting membrane and the lower boundary of the outer nuclear layer (indicated as RNFL on the image by the manufacturer's software). **(D)** Vertical B-scan with yellow squares indicating the position of the points of measurement along the scan. **(E)** Horizontal B-scan with yellow squares indicating the position of the points of measurement along the scan.

approximately 400 μm toward the center of the optic disc along the line of the scan (Fig. 1B–D).

Electroretinography

Full-field ERG under photopic conditions was performed in a subset of animals (r-sham, n = 5; r-mTBI, n = 3) at 10 weeks. For this test, animals were anesthetized with an intraperitoneal injection of a mixture of ketamine (60 mg/kg) and xylazine (5 mg/kg). Their pupils were dilated with 1% tropicamide (Alcon Laboratories) and 5% phenylephrine hydrochloride (EyePhrine), and the animals were placed on a heating pad attached to a Gaymar T/Pump TP650 (Stryker, Inc., Kalamazoo, MI). An Espion E^2 system with Color Dome stimulator (Diagnosys, Lowell, MA) was used to generate stimuli and record data. A mouse contact lens electrode with an embedded gold loop (Mayo Corporation, Inazawa, Japan) was used as an active electrode; a subdermal stainless steel needle electrode placed in the midline of the skull between the eyes was used as a reference. Four different types of stimuli were delivered on a white background with a luminance of 30 cd/m^2, that is, white flashes of 2 different intensities (30 cd.s/m^2 and 300 cd.s/m^2) and green flashes (λ_{max} = 510 nm) of 2 different intensities (30 cd.s/m^2 and 60 cd.s/m^2). All flashes were delivered at a rate of 1 Hz, and the period analyzed was 300 milliseconds. The signal was amplified at least 10,000 times, and filter settings were 0.1 to 1,000 Hz. The photopic b-wave was measured from the trough of the a-wave to the peak of the b-wave, whereas the photopic negative response (PhNR) was measured at the lowest point after the b-wave peak within the time interval 100 to 250 milliseconds.

Statistical Analysis

Optical coherence tomography measurements were analyzed using 2-way analysis of variance (ANOVA), including the Sidak multiple comparison test for individual points when an interaction between the 2 factors (i.e. location of the measurement and treatment effect) was present. For ERG analysis, results from both eyes were averaged, and the average values were used for statistical comparison. Similarly, morphometric measurements of optic nerve diameters from the left and right optic nerves were averaged, and the averaged values are compared. Cellularity analysis of the optic nerves and inner retina used only 1 eye per optic nerve per subject. For OCT retinal thickness analysis, 1 eye per mouse was randomly selected and included in the analysis. For RGC counts and RGC density comparison within the 4 circular areas, results from both eyes were aggregated. In this case, to account for the unbalanced sample size and the interocular correlation, a mixed-model ANOVA was used on log-transformed data, with the mouse ID nested under treatment groups and considered a random effect. Comparison between groups for other measures was done using the Mann-Whitney test. A value of 0.05 was used as a significance level to reject the null hypothesis in all tests.

GraphPad Prism 6.0 (Graph Pad Software Inc., La Jolla, CA) and Sigma Plot 8.0 (Systat Software, Inc., San Jose, CA) were used for graphing purposes. GraphPad Prism was used for most of the statistical analysis; JMP version 8.0.2.2. (SAS Institute Inc., Cary, NC) was used for mixed-model ANOVA analysis.

RESULTS

Retinal Thickness in the Peripapillary Region

Spectral-domain OCT was used to analyze the TRT and the IRT obtained with the circular scan in the peripapillary retina at 10 weeks after injury (Figs. 1A, B; 2). Both measures of retinal thickness were compared in any 8 sectors in mice after r-sham versus r-mTBI.

The average value of the TRT across all sectors in r-sham mice was 255.2 ± 1.5 μm (mean ± SE), whereas the average

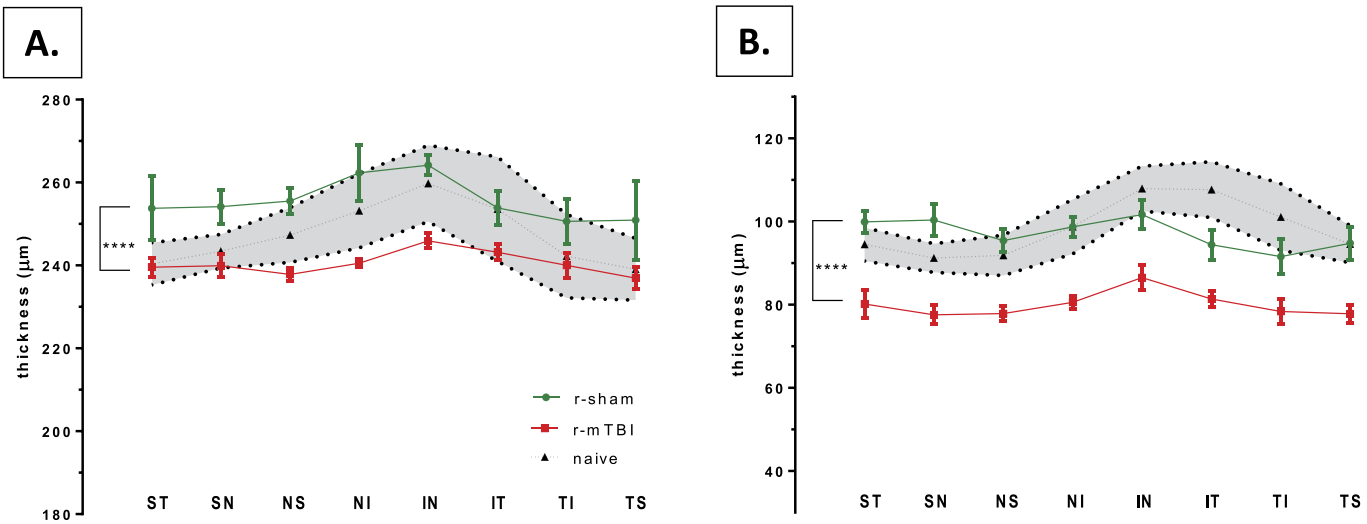

FIGURE 2. Retina thickness measured by a circular B-scan. Eight-sector average circular scan measurements for total **(A)** and inner **(B)** retinal thicknesses. Mean values ± SEM are presented for each segment for the repetitive anesthesia alone (r-sham), r-mTBI, and naive groups. Gray area indicates mean values ± 95% confidence interval for the naive mice. Asterisks indicate the level of significance between mTBI and sham (**** $p < 0.0001$; 2-way ANOVA). IN, inferior nasal; IT, inferior temporal; NI, nasal inferior; NS, nasal superior; SN, superior nasal; ST, superior temporal; TI, temporal inferior; TS, temporal superior.

value of the TRT in mice after r-mTBI was 239.0 ± 1.6 μm; the observed overall decrease in thickness was significant ($p < 0.0001$, 2-way ANOVA; Fig. 2A). Because an interaction between position and thickness accounted for a very small amount of the total variance, which was not statistically significant, a post hoc analysis of individual differences at a different sector level was not conducted.

We next performed segmentation and measurement of the inner retina thickness to address the question of whether the observed generalized decrease in TRT was caused by a process affecting all retinal layers or was specially restricted to thinning of the inner retina. Measurements of IRT across the 4 quadrants in r-sham mice resulted in an average value of 97.6 ± 1.0 μm; in r-mTBI mice, the mean value was 74.2 ± 1.4 μm, indicating a 24% decrease in thickness. This difference was significant ($p < 0.0001$, 2-way ANOVA; Fig. 2B). Thus, the entire difference in TRT between the 2 groups can be explained by the thinning of the inner retina after r-mTBI. As with overall thinness measurements, no interaction was observed between measurement position and thickness.

Of note, the average values for the retinal thickness under both conditions (full retinal thickness and IRT) in naive mice were much closer to the values of r-sham mice than to the values for r-mTBI mice (Fig. 2). When tested with 2-way ANOVA, the difference in retinal thickness between naive mice and mice after r-mTBI was significant for both comparisons ($p < 0.0001$).

Retinal Thickness in the Midperiphery

In addition to the measurement and analysis of the peripapillary region, SD-OCT was used to evaluate TRT and IRT in the midperiphery using vertical and horizontal line B-scans

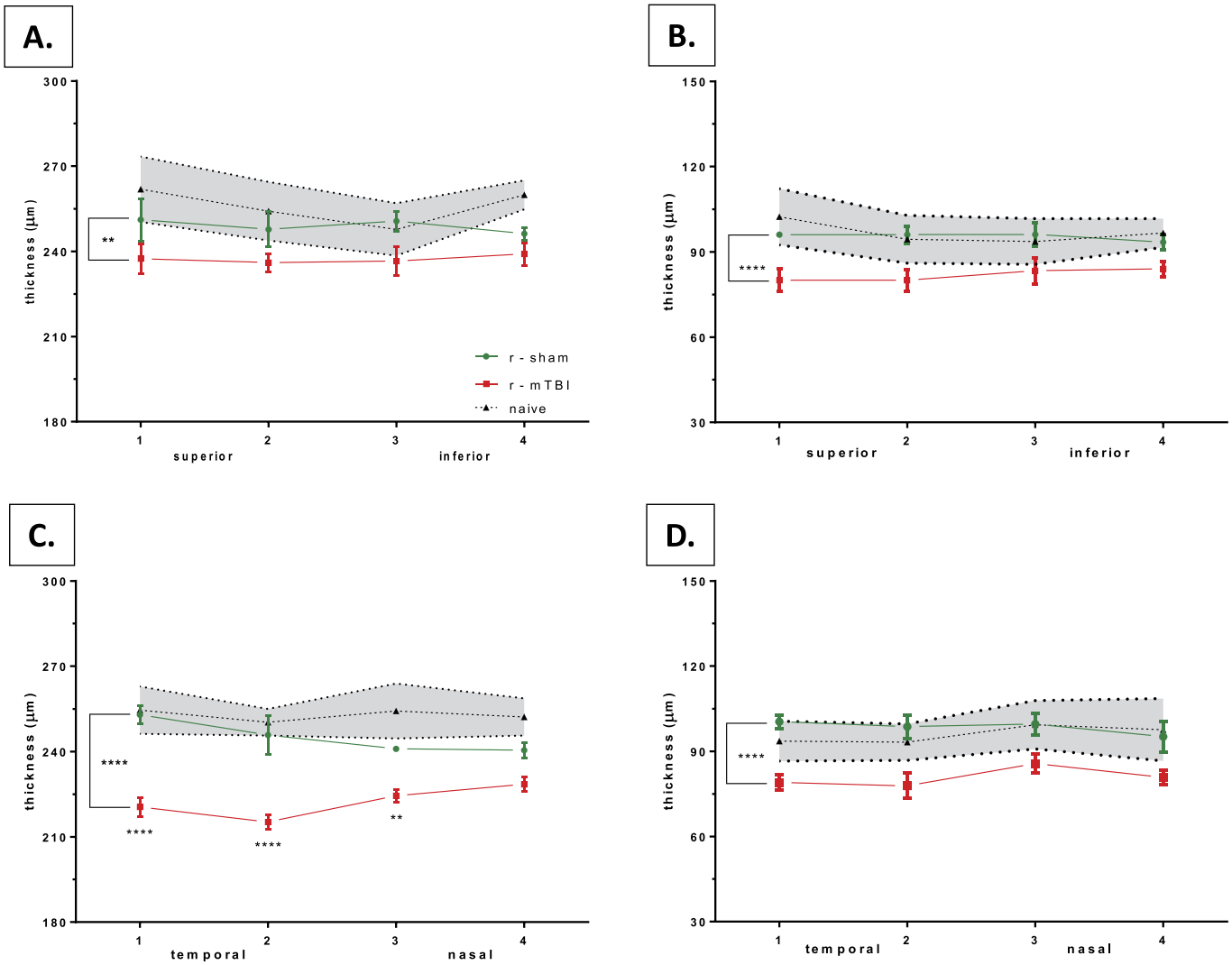

FIGURE 3. Retina thickness measured by a vertical and horizontal B-scan. Average vertical B-scan measurements for total **(A)** and inner **(B)** retinal thicknesses. Average horizontal B-scan measurements for total **(C)** and inner **(D)** retinal thicknesses. Mean values ± SE are presented for each segment for the repetitive anesthesia alone (r-sham), r-mTBI, and naive groups. Gray areas indicate mean values ± 95% confidence interval for the naive mice. Asterisks indicate the level of significance between mTBI and sham (2-way ANOVA).

(Fig. 3). The average TRT along the vertical B-scan of r-sham mice was 250.6 ± 1.8 μm, a value that was considerably higher compared with the corresponding value from r-mTBI mice of 237.8 ± 1.0 μm ($p < 0.0001$, 2-way ANOVA).

Inner retinal thickness along the vertical scan also differed between the 2 groups. Thus, the average IRT for r-sham mice was 97 ± 1.5 μm, whereas the same measure for r-mTBI mice was 83.1 ± 0.3 μm (a 14.3% thinning, $p < 0.0001$, 2-way ANOVA). No interaction between position and thickness was observed either for TRT or IRT and, therefore, post hoc multiple comparisons were not explored.

Measurements along the horizontal B-scan provided results similar to the one obtained from the vertical scan. Thus, the average TRT from r-sham versus r-mTBI mice was 242.8 ± 2.5 μm versus 221.8 ± 2.6 μm ($p < 0.0001$, 2-way ANOVA). Because an interaction between position and thickness was considered significant ($p = 0.007$), the Sidak multiple comparison test was conducted and confirmed that the retinal thickness in all 4 points differed between the groups to variable degrees of significance (from $p < 0.01$ to $p < 0.0001$; Fig. 3C).

As in the case of the vertical scan, IRT measurements along the horizontal scan also differed between the 2 groups. The average IRT for r-sham mice was 97.8 ± 1.1 μm, whereas the same measure for r-mTBI mice was 80.1 ± 0.6 μm (18.1% thinning, $p < 0.0001$, 2-way ANOVA; Fig. 3D). There was no interaction between position and thickness by 2-way ANOVA analysis.

As with the peripapillary measurements, the average values for TRT and IRT of naive mice were much closer to the values of r-sham mice compared with the values for r-mTBI mice. When tested with 2-way ANOVA, the differences in

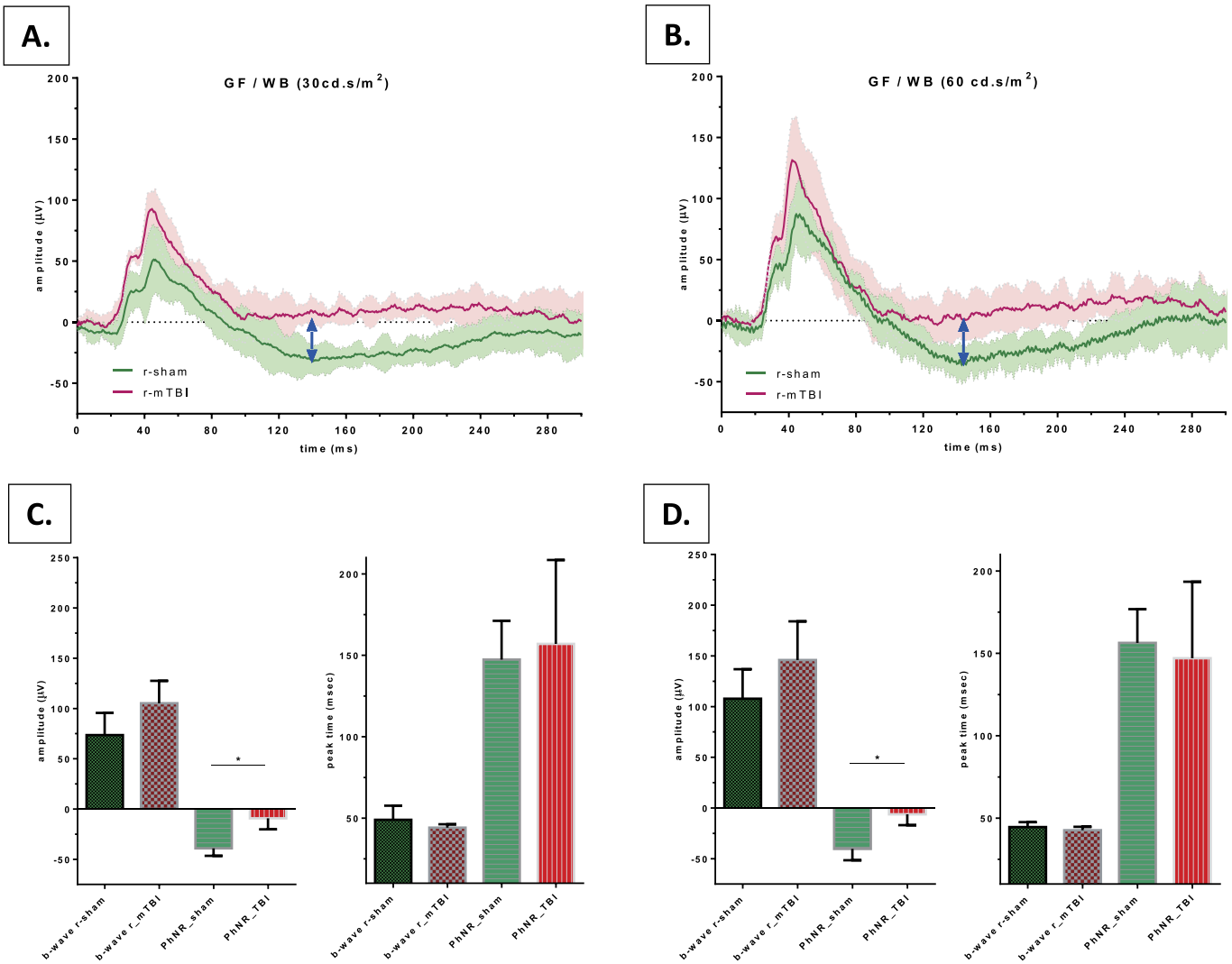

FIGURE 4. Electroretinography traces and amplitude and timing measures of the main ERG components under stimulation with green light. **(A, B)** Recordings obtained under green flash stimulation on a white background. The stimulus strength is indicated in brackets. Average of the traces is presented in bold lines, and 95% confidence intervals are presented in shaded areas. Blue arrows indicate the place and size of the PhNR amplitude. GF, green flash; WB, white background (for details, see Materials and Methods). **(C, D)** Amplitudes and peak times of the main ERG components. Bars represent mean values; error bars represent SE. Intergroup comparisons were performed with Mann-Whitney test (* $p < 0.05$). r-sham, repetitive anesthesia alone.

retinal thickness between naive mice and mice after r-mTBI were statistically significant for all comparisons ($p < 0.0001$).

Changes in Photopic ERG Parameters

At 10 weeks after injury, full-field ERG responses were recorded under 4 different photopic conditions. In all 4 stimulus conditions, the initial part of the ERG response (a-wave, b-wave, oscillatory potentials) was similar in timing and overall shape between r-sham and r-mTBI mice. However, the shape of the PhNR differed markedly between the 2 groups, with r-mTBI mice exhibiting much less negativity (i.e. lower amplitude of the PhNR) versus the r-sham mice (Fig. 4; Figure, Supplemental Digital Content 1, http://links.lww.com/NEN/A568). Amplitude comparison confirmed that the PhNR amplitude was significantly different between the 2 groups for all 4 stimulus conditions; the r-sham mice showed a higher amplitude compared with the r-mTBI mice ($p < 0.05$, Mann-Whitney *t*-test; Fig. 4A, C). Although some tendency was observed for the other ERG components, such as the b-wave, to be higher in the r-mTBI group compared with those in the r-sham group, this difference was not significant ($p > 0.05$, Mann-Whitney *t*-test).

The ERG b-wave peak times were not different between the 2 groups for any of the 4 conditions tested. Similarly, except for the stimulus condition using white stimulus 30 cd.s/m^2 on a white background, the peak times of the PhNR were not different between the 2 groups (Fig. 4; Figure, Supplemental Digital Content 1, http://links.lww.com/NEN/A568). A visual inspection of the ERG traces under the stimulus condition where the peak time difference was significant (Figure, Supplemental Digital Content 1, http://links.lww.com/NEN/A568, part C) indicates an early, albeit small, trough for the PhNR in the r-mTBI group and a relatively flat trace appearance after that for the duration of the epoch. Thus, the difference in timing may be artifactual because of the relatively early flattening of the trace, which makes a precise determination of a negative trough difficult.

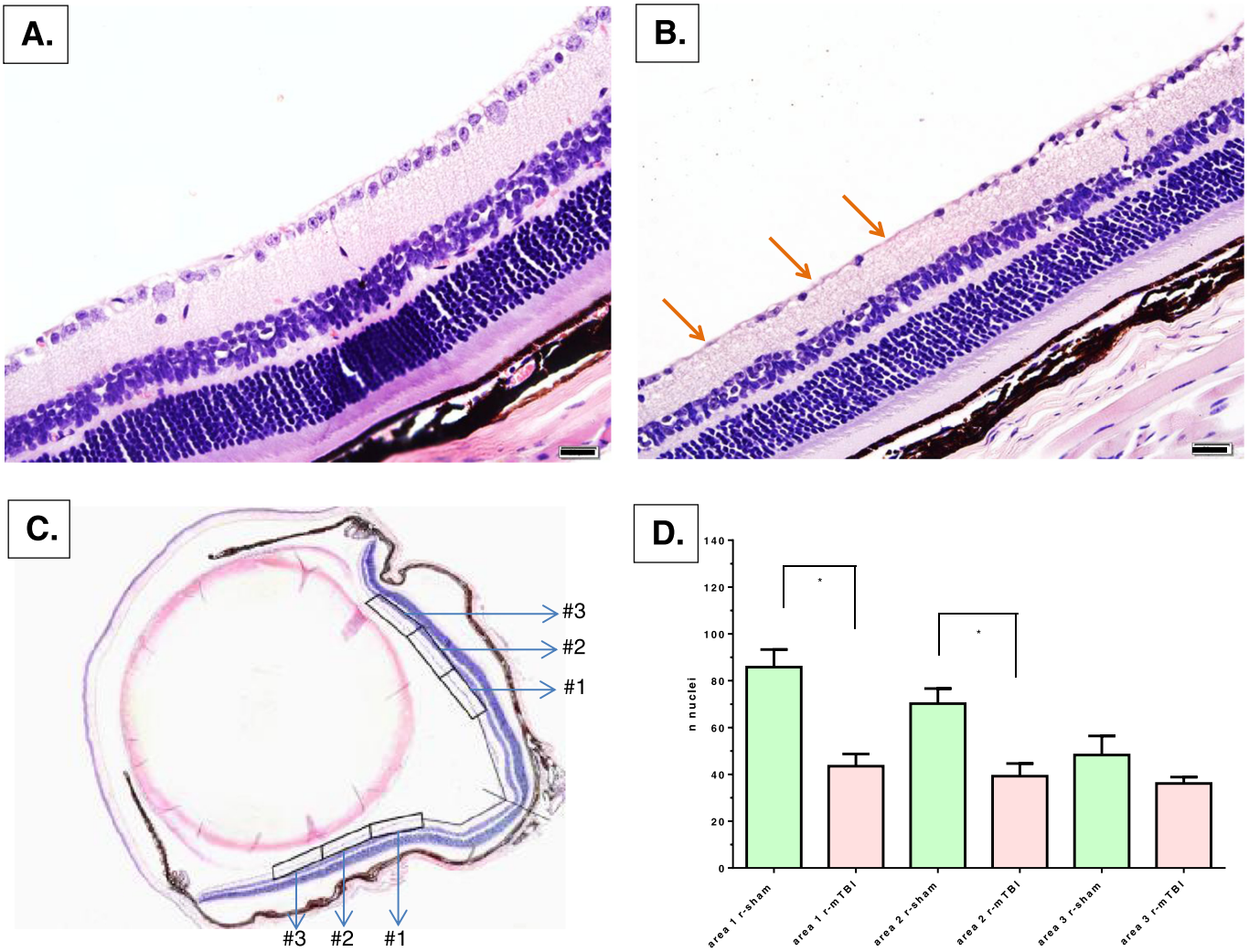

FIGURE 5. Cross sections and analysis of the cellularity in the RGC layer. Representative cross sections of equivalent areas in the upper retina from mice 10 weeks after anesthesia alone (r-sham) **(A)** and after r-mTBI **(B)**. Areas of reduced cellular density in the RGC layer are indicated with arrows. Scale bar = 20 μm. **(C)** Schematic diagram of an eye cross section indicating the positions of the measurement areas 1 to 3. **(D)** Average number of nuclei per area in GCL in the 2 groups. Intergroup comparisons were performed with Mann-Whitney test (* $p < 0.05$).

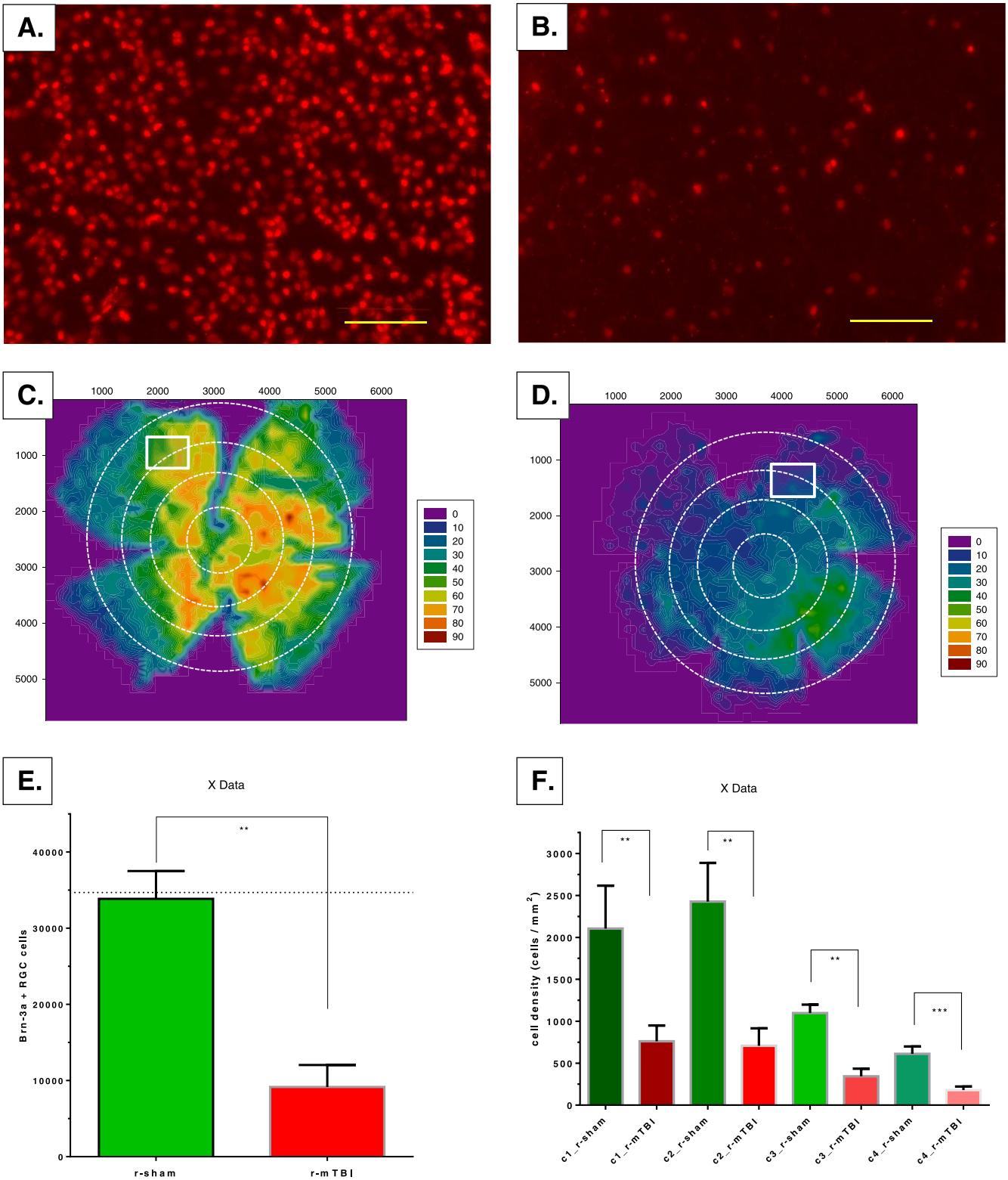

FIGURE 6. Representative images of retina flat mounts and results from RGC counts. Representative images from the upper retina of a mouse after repetitive anesthesia alone (r-sham) **(A)** and r-mTBI **(B)**. Retinal ganglion cells are labeled with anti–brain-specific homeobox/POU domain protein 3A (Brn-3a) antibody. Scale bar = 100 μm. Representative isodensity maps of retinas after r-sham **(C)** and r-mTBI **(D)**. **(E)** Comparison between the total number of Brn-3a–positive RGCs in the 2 groups. **(F)** Comparison between the cell density (in cells per square millimeter) in each circle or circular segment between r-sham and r-mTBI. ** $p < 0.01$.

Retinal Appearance and Cellularity in RGC Layer

Retinas from both r-sham and r-mTBI groups generally appeared normal on histologic preparations through the vertical meridian, whereas areas of reduced cellularity in the RGC layer were noted in sections from r-mTBI mice (Fig. 5A, B). This observation prompted an image analysis to quantify the perceived differences in cellularity. Three adjacent areas, each corresponding in size to 1 microscopic field at magnification 400×, were imaged and analyzed in the superior and inferior parts of the retina (Fig. 5C). Image analysis showed a significant decrease in the number of cells in the RGC layer in the r-mTBI group compared with that in the r-sham group for the 2 areas closer to the optic disc ($p < 0.05$, Mann-Whitney test). The same tendency was also observed in the third most distant area, but it did not reach statistical significance (Fig. 5D).

Ganglion Cell Counts From a Flat Mount

The total number of Brn-3a–positive RGC in flat mounts after repeated anesthesia (r-sham) was estimated at 33,858 ± 3,653. This number is similar to one determined by Galindo-Romero et al (15) (34,627 ± 1,821) using the same method for wild-type pigmented C57BL/6 mice and to those of other investigators using different methods (17).

Visual inspection of individual fields and isodensity maps of RGCs generated from the quantitative data obtained from RGC counting demonstrated reduced cellular density in retinas after r-mTBI compared with retinas after r-sham (Fig. 6A–D). The comparison between the total number of RGCs between the 2 groups indicated an approximate 67% reduction in eyes after mTBI to a total number of 11,062 ± 3,287 ($p = 0.002$, mixed-model ANOVA; Fig. 6E). This difference

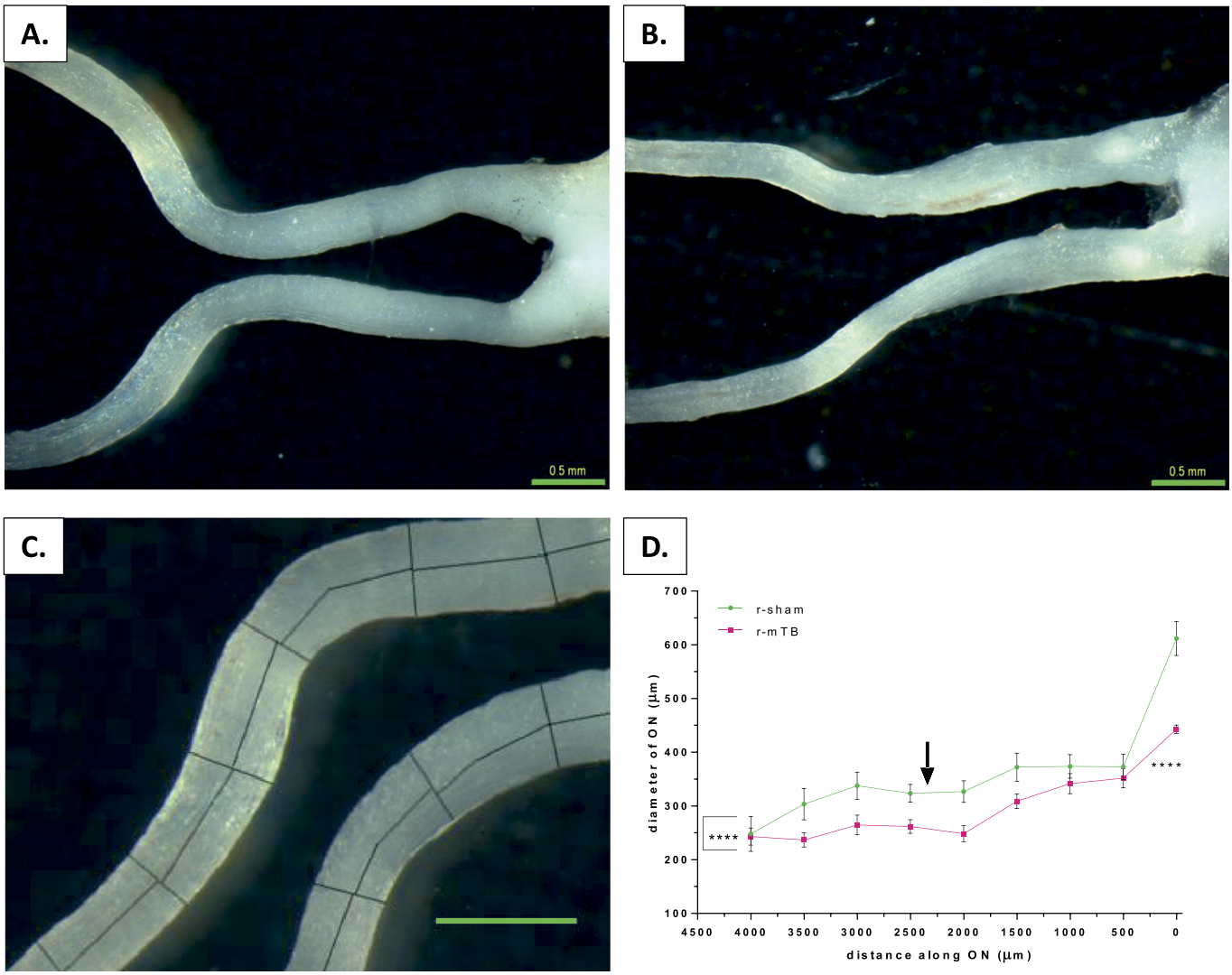

FIGURE 7. Representative images of optic nerve preparations and optic nerve diameter measurements. Optic nerve preparation from mice 13 weeks after repetitive anesthesia alone (r-sham) **(A)** and r-mTBI **(B)**. **(C)** Optic nerve diameter measurement method; lines along the length of the optic nerve indicate longitudinal measurements; perpendicular lines indicate optic nerve diameter measurement (scale bar = 500 µm). **(D)** Mean values for optic nerve diameters from the 2 groups; black arrow indicates the approximate location of the intracanalicular part of the nerve. **** $p < 0.0001$.

was also significant for any of the 4 circular areas ($p < 0.01$ for areas 1–3, $p < 0.001$ for area 4, mixed-model ANOVA; Fig. 6F). The percent decrease in cell density was approximately the same for each circular area (63.8%, 70.8%, 68.7%, and 70.7% for areas 1–4, respectively), indicating diffuse RGC loss, with no difference in the pattern of cell loss between the central and more peripheral retinal areas.

Morphometry and Histopathology of Optic Nerves

Optic nerves of mice at 13 weeks after injury were extracted and imaged to obtain an estimate of possible changes in their diameter along the length of the nerve (Fig. 7A–C). Overall, the diameter of the optic nerves in mice after r-mTBI was significantly decreased compared with the diameter of optic nerves after r-sham ($p < 0.0001$, 2-way ANOVA; Fig. 7D). Two-way ANOVA analysis indicated a significant interaction between location and the size of optic nerve diameter ($p = 0.01$), and therefore, Sidak multiple comparison test was applied. The only significant decrease in mean diameter was observed at the point of juncture between the optic nerve and the chiasm (27.5% thinning, $p < 0.0001$).

Routine H&E stains revealed the presence of a larger number of cell nuclei in longitudinal sections of the optic nerve after r-mTBI compared with r-sham or naive mice (Fig. 8A–C). These lesions showed mononuclear cell infiltrates and foamy macrophages (Fig. 8D). These lesions were multifocal and bilateral (Figure, Supplemental Digital Content 2, http://links.lww.com/NEN/A569). In addition, LFB/CV stain demonstrated local areas of reduced LFB staining in optic nerves after r-mTBI compared with a typical uniform stain appearance after r-sham, or in naive mice, suggestive of local areas of demyelination (Fig. 9A–C). Furthermore, some areas resembled "cavernous degeneration" (Fig. 9D). The optic nerve examples from mice after r-mTBI

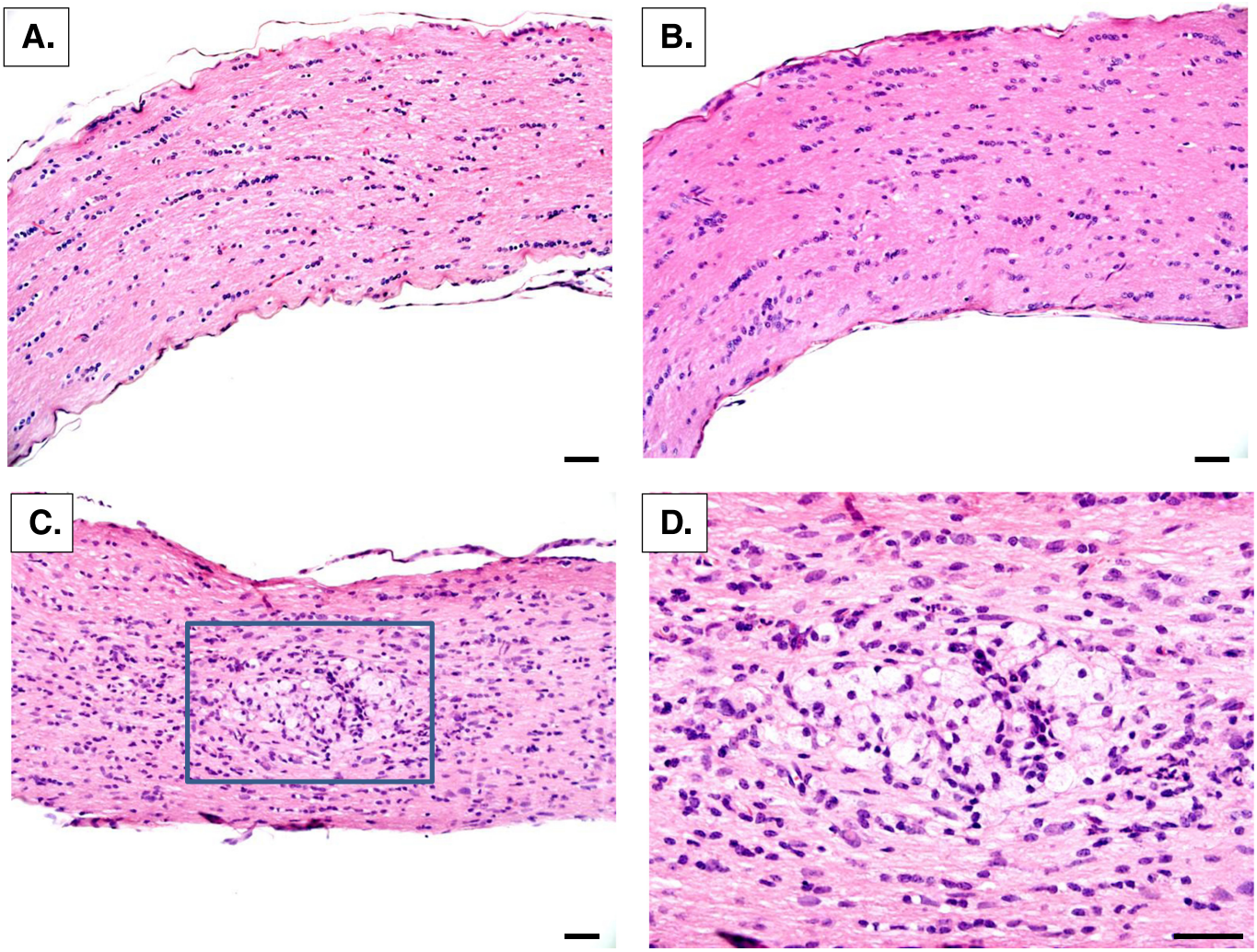

FIGURE 8. Representative longitudinal cross sections of optic nerves at 13 weeks after injury stained with H&E. Samples from naive **(A)**, repetitive anesthesia alone (r-sham) **(B)**, and r-mTBI **(C)** mice. There is an overall increase in the number of nuclei in the optic nerve of the (r-mTBI) mouse compared with the other mice. Original magnification: 200×. Scale bar = 20 μm. **(D)** Higher magnification of the boxed region in **(C)** reveals areas of foamy macrophages with a few adjacent clusters of mononuclear inflammatory cells suggestive of "cavernous degeneration." Original magnification: 400×. Scale bar = 20 μm.

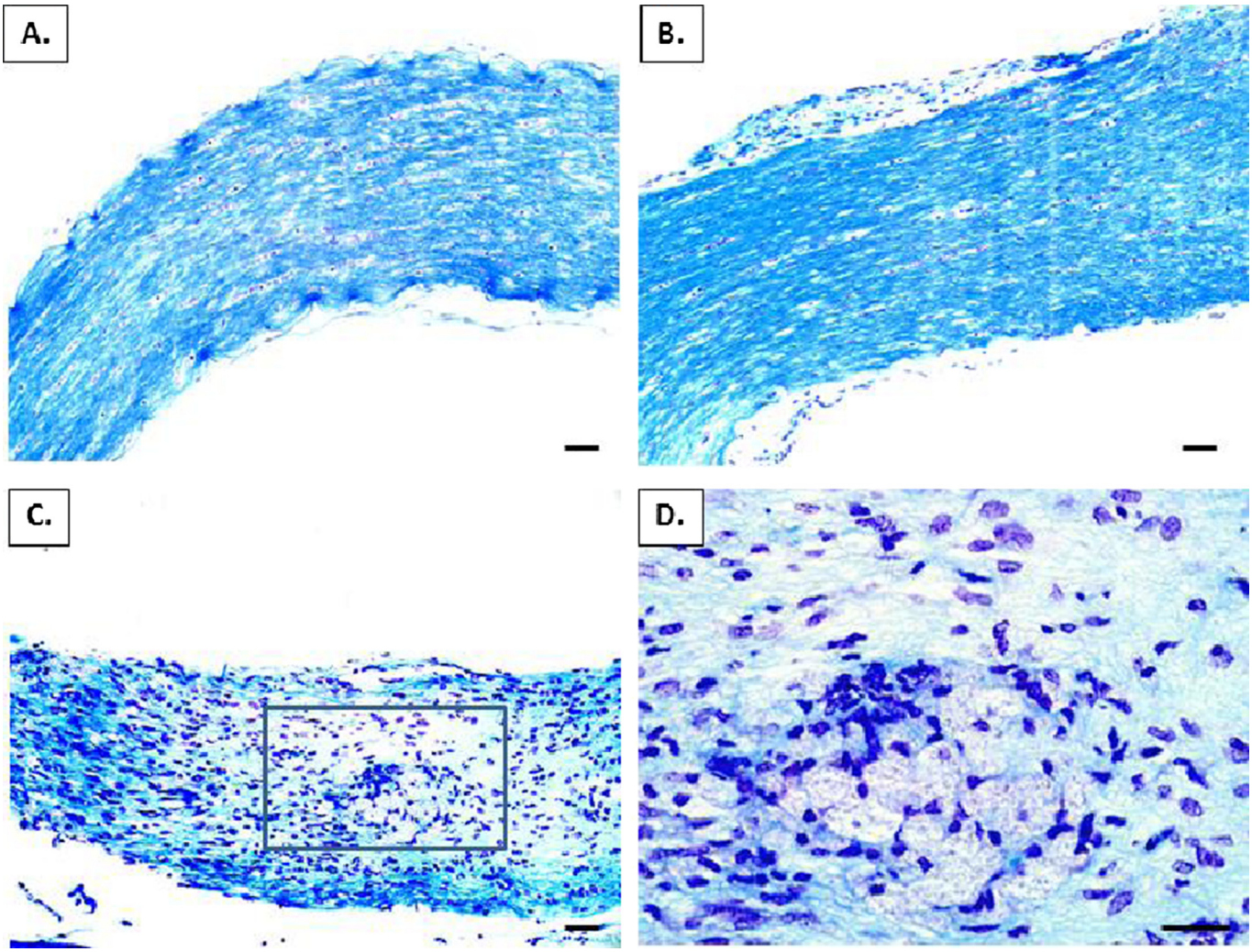

FIGURE 9. Representative longitudinal cross sections of optic nerves at 13 weeks after injury stained with Luxol fast blue/cresyl violet. Nerves from naive **(A)**, repetitive anesthesia alone (r-sham) **(B)**, and r-mTBI **(C)** mice. Original magnification: 200×. Scale bar = 20 μm. **(D)** Higher magnification of the boxed region in **(C)** reveals an area of reduced Luxol fast blue staining indicating focal demyelination and a similar "cavernous degeneration" appearance as in Figure 8D. Original magnification: 400×. Scale bar = 20 μm.

respectively) were from different animals, supporting the reproducibility of this observation.

Results from the image analysis of H&E-stained sections demonstrated that the mean cellular density in optic nerves after r-mTBI was 4,361 ± 276 cells/mm^2 versus 2,892 ± 85 cells/mm^2 after r-sham, a 33.7% increase; this difference was significant ($p < 0.0001$, Mann-Whitney test) (Fig. 10). The average cellular density in optic nerves of naive mice was very close to that observed in r-sham mice, 2,698 ± 152 cells/mm^2, and was also significantly different compared with that observed in r-mTBI mice ($p < 0.0001$, Mann-Whitney test).

Immunohistochemistry of Optic Nerves

To investigate further what could be the source of the increased cellularity observed in optic nerves after r-mTBI, optic nerves were stained for Iba-1 and GFAP to detect microglia and astrocytes, respectively. Ionized calcium-binding adaptor molecule 1 stain revealed an increased expression in r-mTBI staining for GFAP also demonstrated a marked upregulation in GFAP expression, indicating astrocytosis (Fig. 11C, D).

DISCUSSION

Subjective visual complaints and visual impairment can be a relatively frequent consequence of TBI, although good epidemiologic data are lacking (5, 6, 18–20). Thus, self-reported visual complaints and symptoms such as blurry vision and photosensitivity and visual impairment such as visual acuity loss and visual field defects are reported (21). Pathologic findings in the optic nerve after moderate to severe TBI have been well documented and include ischemic necrosis and shearing lesions most often localized near the optic foramen (20). Another postmortem study found axonal injury of varying severity in all cases and concluded that the severity of injury to the optic pathways did not always reflect severity of axonal injury elsewhere in the brain (22). Much less is known about the consequences for the optic nerve and the retina from mild

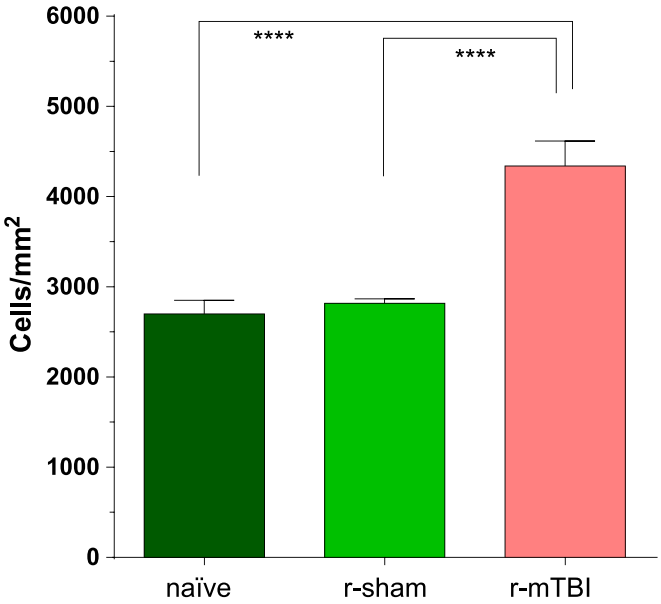

FIGURE 10. Average cell density in longitudinal sections of the optic nerves from mice at 10 weeks after repetitive anesthesia alone (r-sham) and r-mTBI and from naive mice. Group comparisons of average cell density from r-sham and r-mTBI mice and between naive and r-mTBI mice were significant. **** $p < 0.0001$.

(either single or repetitive) TBI or the mechanisms of visual impairment associated with it. Our goal was to investigate the effects of r-mTBI on the mouse optic nerve and the retina at 10 to 13 weeks after injury using our recently developed mouse model of mTBI, which demonstrates neuropathologic and neurobehavioral changes consistent with those in human TBI (10, 12).

Retinal Structural Changes

We observed thinning of the inner retina and decreased cellularity in the RGC layer in mice after r-mTBI compared with mice after repeated anesthesia alone. This was also associated with a dramatic almost uniform decrease in the number of Brn-3a–positive RGCs throughout the retina. The observed decrease in RGC numbers suggests that the thinning of the inner retina observed by SD-OCT in the present study is most likely caused by thinning of the RNFL and is likely correlated with a decrease in optic nerve axons. This hypothesis is supported by work from Camp et al (23) who found that mice with a targeted disruption of *Brn-3b* gene showed a strong correlation between IRT change as measured by SD-OCT and RGC counts. Similarly, significant RNFL thinning was observed in mice with spontaneously elevated intraocular pressure (IOP) and was associated with decreased ERG response (24).

The similarity between IRT reduction across all 4 quadrants and 8 sectors in the peripapillary region and the similarity of the proportion of RGC loss between the center and the periphery suggest a diffuse neurodegenerative process. Diffuse RGC loss is well documented after optic nerve transection in rats (25–28) and partial optic nerve crush in mice (29–31). Retinal ganglion cell degeneration and subsequent loss were also demonstrated after optic nerve stretch in guinea pigs (32, 33) and mice (34) or after partial optic nerve crush in rats (35, 36). Thus, despite some recent negative results (37), the majority of the published studies document RGC degeneration and loss even without complete disruption of optic nerve fibers.

The amount of RGC loss in our study (~67% at 13 weeks after injury) corresponds to a level between mild and very mild direct optic nerve injury in rats as reported by Yoles and Schwartz (38). In that context, the RGC loss after complete optic nerve transection is reported to be much faster, that is, 90% of the RGCs died by Day 14 in rats (27) and 85% by Day 21 in mice (15). In future studies, we will pursue the temporal dynamics of the RGC loss after TBI for better comparison with RGC loss after direct optic nerve crush or transection.

Retinal Functional Changes Recorded by ERG

Photopic negative response is an ERG component that originates from the RGCs (39) and was shown to decline after optic nerve transection and also after IOP elevation in rodents and monkeys (39–43) and in a mouse model of dominant optic atrophy (44). The shape of the PhNR in our mouse study was similar to those previously reported in rodent studies (40, 42, 44). Our results demonstrate a decline in the amplitude of PhNR under all 4 stimulus conditions at 10 weeks after injury, indicating widespread RGC dysfunction. Under one of the recorded stimulus conditions (green flash of 30 cd.s/m^2 on a white background), the reduction in the PhNR amplitude in mice after r-mTBI compared with the PhNR amplitude in mice after r-sham (76.4%) was similar to the reduction in total number of RGCs (67.3%). Further studies are warranted to determine whether this level of correlation between functional and structural deficits in the mouse retina after r-mTBI holds for other time points and stimulus conditions.

In general, deterioration of RGC function after optic nerve trauma is well documented, but there are few analogs for effects on the PhNR from clinical studies. Notable examples include a small series report of a substantial (~50%) decrease in PhNR in 3 cases of unilateral optic neuropathy with little effect on the photopic a- and b-waves (45). Similarly, PhNR has demonstrated very good diagnostic sensitivity, being depressed in 4 of 5 cases after traumatic compression of the optic nerves, whereas photopic ERG a- and b-waves remained normal (43). In terms of correspondence between ERG and structural measures, such as OCT, a good correlation between the reduction in PhNR amplitude and a decrease in RNFL thickness was also demonstrated in patients with multiple sclerosis (46), supporting the sensitivity of this test to optic nerve/RGC dysfunction. Because ERG is well suited for an objective evaluation of retinal function and for estimating the safety and efficacy of new treatments in clinical and preclinical settings (47), PhNR may be a useful full-field ERG component to follow the progression of visual function deterioration related to TBI and efficacy of treatments designed to mitigate its negative effects.

Optic Nerve Changes

Cellular proliferation in the optic nerve was previously demonstrated after IOP elevation in rats, and the level of this proliferation after "mild" injury was larger compared with the proliferation observed after optic nerve transection (48).

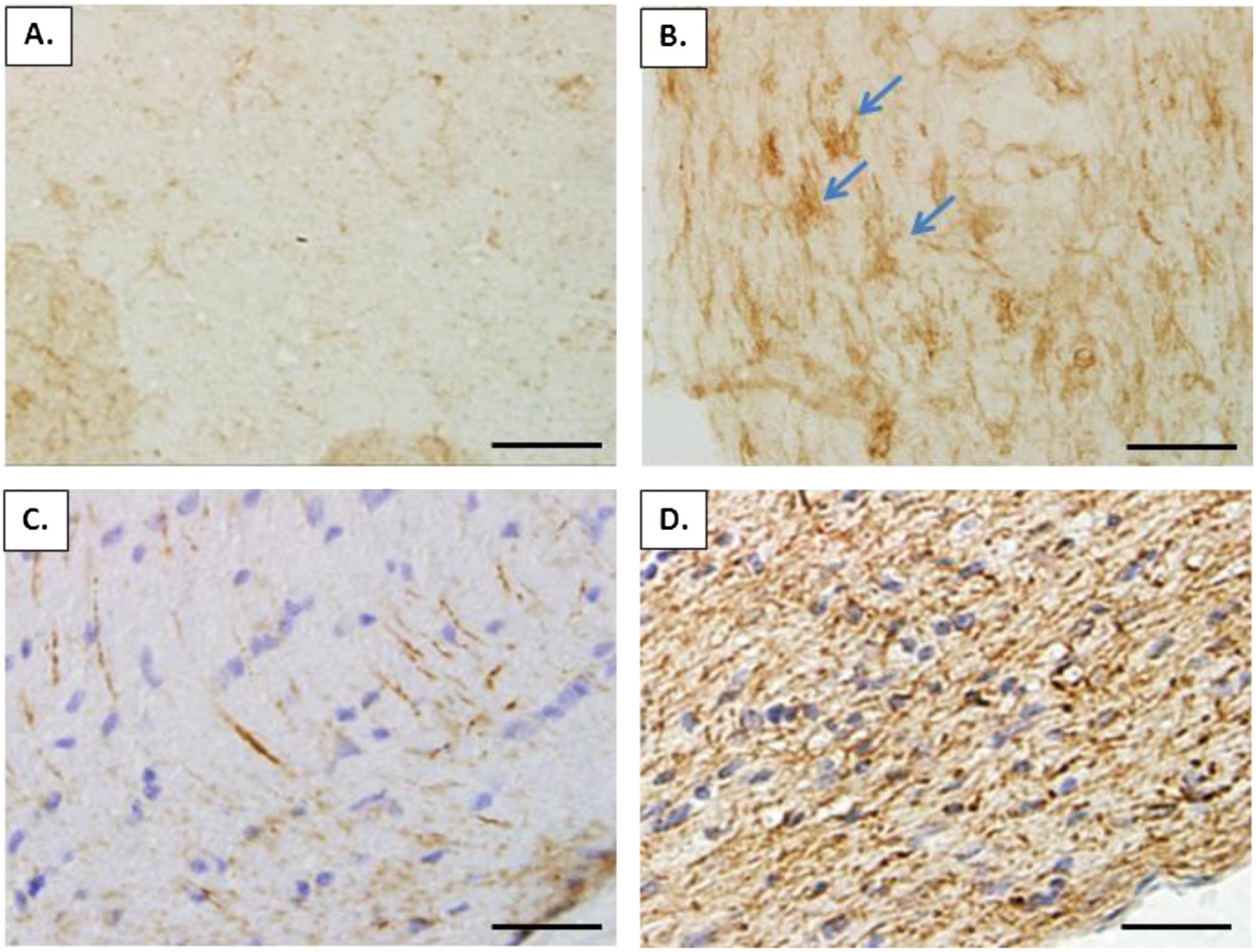

FIGURE 11. Microglial and astroglial activation in optic nerve after r-mTBI. Ionized calcium-binding adaptor molecule 1 immunostain of longitudinal sections of optic nerves 13 weeks after repetitive anesthesia alone (r-sham) **(A)** and r-mTBI **(B)**. Blue arrows indicate activated microglia. Glial fibrillary acidic protein (GFAP) immunostain of longitudinal sections of optic nerves at 13 weeks after r-sham **(C)** and r-mTBI **(D)**. There is prominent GFAP immunoreactivity indicating astrocytosis in **(D)**. Original magnification: 400×. Scale bar = 50 μm.

Similar findings of increased cellularity in the optic nerve accompanied by atrophy, astrogliosis, and fragmentation of axons were reported in optic nerve atrophy after IOP elevation in the DBA/2NNia substrain of mice with inherited angle-closure glaucoma (49).

In addition to cell proliferation, leukocyte infiltration of the optic nerve after the injury would be likely. Thus, ED1-positive monocyte/macrophages were prominent throughout the optic nerve at 8 and 16 weeks after optic nerve transection (50). Similarly, T cells showed transiently increased accumulation up to 3 weeks after optic nerve crush in rats (51). The presence of monocytes, macrophages, and T cells may also help protect the retina from secondary degeneration occurring after optic nerve crush (52). It was outside the scope of the present study to quantify the proportion of cellular proliferation versus cellular infiltration, an area for further studies.

We observed areas containing foamy macrophages and with an overall appearance of so-called "cavernous degeneration" in nerves at 13 weeks after r-mTBI. This term was applied to findings in the optic nerve of owl monkeys after acute experimental glaucoma (53) and has since been used to describe lesions in rats after locally induced photochemical ischemia of the optic nerve (31). Similar lesions with foamy macrophages have been observed in postmortem optic nerve specimens from humans with ischemic optic neuropathy (54). In view of reports of similar findings associated with optic nerve trauma and injury, the localized foamy macrophages and demyelination observed in the present study were not unexpected. Regional demyelination was observed after induction of inflammation in the optic nerve by immunization with myelin proteolipid protein peptide (55) or after optic nerve crush (56) or associated with anterior ischemic optic neuropathy (56) in the mouse. Localized demyelination was also observed after an optic nerve stretch in the guinea pig (57–59). To the best of our knowledge, this is the first report of this type of lesion in optic nerves after r-mTBI in the mouse.

We demonstrated increased immunoreactivity for microglia and astrocytes in the optic nerve at 10 to 13 weeks after TBI. Microglia and/or macrophage activation was previously identified in the injured optic nerves 1 to 4 weeks after optic nerve stretch injury in mice (37).

Comparison With Findings in Other Models of TBI

A wide variety of different preclinical models are currently used for studying the effects of different forms of TBI, which in rodents include controlled cortical impact models (60), frontal impact closed-head injury (61), and blast injury (62), each with their own characteristics (63), but neuroinflammation is a consistent feature (64, 65).

Many authors agree that a prominent feature in most TBI models is the finding of diffuse axonal injury (66–70). Diffuse axonal injury is characterized by impaired axoplasmic transport, continued axonal swelling, ultimate disconnection of the axons, and swelling and ischemia in parts of the brain (67, 71). In our model, the presence of diffuse axonal injury was supported by increased amyloid precursor protein and GFAP and IBA-1 immunoreactivity in the corpus callosum and in other regions of the brain acutely (up to 10 days) after r-mTBI in normal young mice (10). Studies from our group focused on the chronic effects of neurotrauma and, to that end, we have characterized neuropathologic changes in our mouse model of mTBI through to a 12-month time point and show progressive neuroinflammation in repetitively versus singly injured mice (12). We have now extended our characterization of this mTBI model to include the visual consequences of TBI and have demonstrated significant consequences to the visual system that likely recapitulate the human condition.

Because the optic nerve is considered to be part of the white matter of the brain, it is logical to assume that diffuse axonal injury would negatively affect its structure and function after TBI. However, very few studies have explored this hypothesis (9), and there are no reports available after r-mTBI. We found histologic abnormalities in the eye and optic nerve at 10 and 13 weeks after r-mTBI in normal mice. To the best of our knowledge, this is the first observation of specific deleterious effects on the visual system after closed-head r-mTBI in the mouse, demonstrating neuronal cell loss in the RGC layer, thinning of the inner retina, decreased full-field ERG PhNR, regional myelin loss, and signs of cavernous degeneration in the optic nerve.

Some similarities exist between the findings described in the present study and the ones described by Mohan et al (9) in a mouse model of single-blast TBI. For example, a decrease in RNFL thickness and reduced cellularity in the RGC layer were noted in both studies at 3 months after injury. At the same time point, some aspects of retinal function reflecting RGC activity (pattern ERG amplitude after blast injury and PhNR amplitude after repetitive blunt injury) were suppressed. Furthermore, structural damage to the optic nerve was found in both instances. Thus, despite the difference in methods and equipment used, both studies confirmed the presence of optic nerve injury and degeneration of the inner retina at 3 to 4 months after TBI. Therefore, visual system dysfunction is likely common after blast and repeated blunt mTBI.

Nonetheless, some differences should be noted between the 2 studies. Most importantly, the nature of the insult was quite different, that is, a single blast versus repetitive blunt trauma. Direct comparative studies between the 2 types of injury are presently lacking, but it can be noted that the repeated mTBI led to more profound and widespread damage to the RNFL (as suggested by SD-OCT findings) compared with results from the single-blast injury. The reason for that and the implied more severe degeneration in the optic nerve after repeated TBI could be the relatively close timing between each of the repeated mTBI (48 hours). This interval was chosen to administer second and subsequent impacts within a window of "brain recovery" (72) and which may also be an insufficient period for the optic nerve edema to subside after the previous injury. Indeed, in another study of central fluid percussion injury in mice, Wang et al (37) showed that swelling of the optic nerve was still present at 48 hours after injury. However, these authors did not find any RGC loss up to 28 days after injury. The reason for this discrepancy may be related to 2 key differences in the experimental approaches (i.e. [37] vs the present study). The first is the difference between single injury versus repeated injury; the second is the analysis at 28 days versus 91 days after injury in the present study. It is worth pointing out that the location of early microglial activation in the optic nerve at 48 hours after a single central fluid percussion injury is similar to the location of the lesions in the present study after r-mTBI (Figure 9A in [37] and Figure, Supplemental Digital Content 2, http://links.lww.com/NEN/A569 in the present study), which underscores the similarities in the mechanism involved. Thus, it can be hypothesized that subsequent TBIs could have a cumulative damaging effect on the optic nerve, spreading the degeneration to the RGC layer.

Significance and Future Directions

The findings of this study underscore the importance of comprehensive evaluation of visual function after mTBI. Together with emerging clinical observations, they emphasize the possibility of a profound and lasting visual dysfunction, particularly after repetitive mild injury, occurring in relatively short intervals. This has considerable implications and relevance to civilian, sport-related, and deployment-related mTBI, where repeated mTBI can occur in a short span of time.

Ongoing studies continue the characterization of the model to further advance our understanding of the visual consequences of mTBI, with a particular focus on the differences between single and repetitive injuries. Use of noninvasive techniques such as SD-OCT and ERG may allow an objective evaluation of the visual function and structure after TBI and can have a direct application in the clinic.

ACKNOWLEDGMENTS

We thank Pharm Optima for its donation of OCT imaging and ERG recording services related to this study. We thank Curtis Margo for helpful comments on an earlier version of this manuscript and review of some optic nerve histologic preparations. We thank Bruce Barton and Gogce Crynen for statistical advice. We thank Mojgan Hosseinipour, Robert Spinelli, Austin Ferro, and Myles Mullan for technical assistance with histology and image analysis. Preliminary

reports of these findings were presented at the Annual Meeting of the Association for Research in Vision and Ophthalmology, Seattle, WA, 2013. The content of this work does not represent the views of the Department of Veterans Affairs or the US Government.

REFERENCES

1. Hyder AA, Wunderlich CA, Puvanachandra P, et al. The impact of traumatic brain injuries: A global perspective. NeuroRehabilitation 2007; 22:341–53
2. Faul M, Xu L, Wald MM, Coronado VG. *Traumatic Brain Injury in the United States: Emergency Department Visits, Hospitalizations and Deaths, 2002–2006*. Atlanta, GA: Centers for Disease Control and Prevention National Center for Injury Prevention and Control; 2010.
3. Binder S, Corrigan JD, Langlois JA. The public health approach to traumatic brain injury: An overview of CDC's research and programs. J Head Trauma Rehabil 2005;20:189–95
4. Saatman KE, Duhaime AC, Bullock R, et al. Classification of traumatic brain injury for targeted therapies. J Neurotrauma 2008;25:719–38
5. Atkins EJ, Newman NJ, Biousse V. Post-traumatic visual loss. Rev Neurol Dis 2008;5:73–81
6. Greenwald BD, Kapoor N, Singh AD. Visual impairments in the first year after traumatic brain injury. Brain Inj 2012;26:1338–59
7. Grubenhoff JA, Kirkwood MW, Deakyne S, et al. Detailed concussion symptom analysis in a paediatric ED population. Brain Inj 2011;25:943–49
8. Suchoff IB, Kapoor N, Ciuffreda KJ, et al. The frequency of occurrence, types, and characteristics of visual field defects in acquired brain injury: A retrospective analysis. Optometry 2008;79:259–65
9. Mohan K, Kecova H, Hernandez-Merino E, et al. Retinal ganglion cell damage in an experimental rodent model of blast-mediated traumatic brain injury. Invest Ophthalmol Vis Sci 2013;54:3440–50
10. Mouzon B, Chaytow H, Crynen G, et al. Repetitive mild traumatic brain injury in a mouse model produces learning and memory deficits accompanied by histological changes. J Neurotrauma 2012;29:2761–73
11. Ojo JO, Mouzon B, Greenberg MB, et al. Repetitive mild traumatic brain injury augments tau pathology and glial activation in aged hTau mice. J Neuropathol Exp Neurol 2013;72:137–51
12. Mouzon BC, Bachmeier C, Ferro A, et al. Chronic neuropathological and neurobehavioral changes in a repetitive mTBI model. Ann Neurol 2013. doi: 10.1002/ana.24064. [Epub ahead of print]
13. Rasband WS. ImageJ. Bethesda, MD: US National Institutes of Health; 1997–2014. Availlable at: http://imagej.nih.gov/ij/.
14. Salinas-Navarro M, Alarcon-Martinez L, Valiente-Soriano FJ, et al. Functional and morphological effects of laser-induced ocular hypertension in retinas of adult albino Swiss mice. Mol Vis 2009;15:2578–98
15. Galindo-Romero C, viles-Trigueros M, Jimenez-Lopez M, et al. Axotomy-induced retinal ganglion cell death in adult mice: Quantitative and topographic time course analyses. Exp Eye Res 2011;92:377–87
16. Huber G, Beck SC, Grimm C, et al. Spectral domain optical coherence tomography in mouse models of retinal degeneration. Invest Ophthalmol Vis Sci 2009;50:5888–95
17. Alarcon-Martinez L, Aviles-Trigueros M, Galindo-Romero C, et al. ERG changes in albino and pigmented mice after optic nerve transection. Vision Res 2010;50:2176–87
18. Lew HL, Garvert DW, Pogoda TK, et al. Auditory and visual impairments in patients with blast-related traumatic brain injury: Effect of dual sensory impairment on Functional Independence Measure. J Rehabil Res Dev 2009;46:819–26
19. Hoyt CS. Brain injury and the eye. Eye (Lond) 2007;21:1285–89
20. Crompton MR. Visual lesions in closed head injury. Brain 1970;93:785–92
21. Brahm KD, Wilgenburg HM, Kirby J, et al. Visual impairment and dysfunction in combat-injured servicemembers with traumatic brain injury. Optom Vis Sci 2009; 86:817–25
22. Perunovic B, Quilty RD, Athanasiou A, et al. Damage to intracranial optic pathways in fatal closed head injury in man. J Neurol Sci 2001; 185:55–62
23. Camp AS, Ruggeri M, Munguba GC, et al. Structural correlation between the nerve fiber layer and retinal ganglion cell loss in mice with targeted disruption of the Brn3b gene. Invest Ophthalmol Vis Sci 2011; 52:5226–32
24. Saleh M, Nagaraju M, Porciatti V. Longitudinal evaluation of retinal ganglion cell function and IOP in the DBA/2J mouse model of glaucoma. Invest Ophthalmol Vis Sci 2007;48:4564–72
25. Sanchez-Migallon MC, Nadal-Nicolas FM, Jimenez-Lopez M, et al. Brain derived neurotrophic factor maintains Brn3a expression in axotomized rat retinal ganglion cells. Exp Eye Res 2011;92:260–67
26. Nadal-Nicolas FM, Jimenez-Lopez M, Salinas-Navarro M, et al. Whole number, distribution and co-expression of brn3 transcription factors in retinal ganglion cells of adult albino and pigmented rats. PLoS One 2012;7:e49830
27. Berkelaar M, Clarke DB, Wang YC, et al. Axotomy results in delayed death and apoptosis of retinal ganglion cells in adult rats. J Neurosci 1994;14:4368–74
28. Peinado-Ramon P, Salvador M, Villegas-Perez MP, et al. Effects of axotomy and intraocular administration of NT-4, NT-3, and brain-derived neurotrophic factor on the survival of adult rat retinal ganglion cells. A quantitative in vivo study. Invest Ophthalmol Vis Sci 1996;37:489–500
29. Leung CK, Weinreb RN, Li ZW, et al. Long-term in vivo imaging and measurement of dendritic shrinkage of retinal ganglion cells. Invest Ophthalmol Vis Sci 2011;52:1539–47
30. Bien A, Seidenbecher CI, Bockers TM, et al. Apoptotic versus necrotic characteristics of retinal ganglion cell death after partial optic nerve injury. J Neurotrauma 1999;16:153–63
31. Wang CH, Wang B, Wendu RL, et al. Protective role of Wallerian degeneration slow (Wld(s)) gene against retinal ganglion cell body damage in a Wallerian degeneration model. Exp Ther Med 2013;5:621–25
32. Maxwell WL, Islam MN, Graham DI, et al. A qualitative and quantitative analysis of the response of the retinal ganglion cell soma after stretch injury to the adult guinea-pig optic nerve. J Neurocytol 1994;23:379–92
33. Mohammed Sulaiman A, Denman N, Buchanan S, et al. Stereology and ultrastructure of chronic phase axonal and cell soma pathology in stretch-injured central nerve fibers. J Neurotrauma 2011;28:383–400
34. Saatman KE, Abai B, Grosvenor A, et al. Traumatic axonal injury results in biphasic calpain activation and retrograde transport impairment in mice. J Cereb Blood Flow Metab 2003;23:34–42
35. Prilloff S, Henrich-Noack P, Sabel BA. Recovery of axonal transport after partial optic nerve damage is associated with secondary retinal ganglion cell death in vivo. Invest Ophthalmol Vis Sci 2012;53:1460–66
36. Dibas A, Oku H, Fukuhara M, et al. Changes in ocular aquaporin expression following optic nerve crush. Mol Vis 2010;16:330–40
37. Wang J, Fox MA, Povlishock JT. Diffuse traumatic axonal injury in the optic nerve does not elicit retinal ganglion cell loss. J Neuropathol Exp Neurol 2013;72:768–81
38. Yoles E, Schwartz M. Degeneration of spared axons following partial white matter lesion: Implications for optic nerve neuropathies. Exp Neurol 1998;153:1–7
39. Viswanathan S, Frishman LJ, Robson JG, et al. The photopic negative response of the macaque electroretinogram: Reduction by experimental glaucoma. Invest Ophthalmol Vis Sci 1999;40:1124–36
40. Li B, Barnes GE, Holt WF. The decline of the photopic negative response (PhNR) in the rat after optic nerve transection. Doc Ophthalmol 2005; 111:23–31
41. Fortune B, Cull GA, Burgoyne CF. Relative course of retinal nerve fiber layer birefringence and thickness and retinal function changes after optic nerve transection. Invest Ophthalmol Vis Sci 2008;49:4444–52
42. Chrysostomou V, Crowston G. The photopic negative response of the mouse electroretinogram: Reduction by acute elevation of intraocular pressure. Invest Ophthalmol Vis Sci 2013;54:4691–97
43. Rangaswamy NV, Frishman LJ, Dorotheo EU, et al. Photopic ERGs in patients with optic neuropathies: Comparison with primate ERGs after pharmacologic blockade of inner retina. Invest Ophthalmol Vis Sci 2004;45:3827–37
44. Barnar AR, Charbel Issa P, Perganta G, et al. Specific deficits in visual electrophysiology in a mouse model of dominant optic atrophy. Exp Eye Res 2011;93:771–77
45. Gotoh Y, Machida S, Tazawa Y. Selective loss of the photopic negative response in patients with optic nerve atrophy. Arch Ophthalmol 2004; 122:341–46
46. Wang J, Cheng H, Hu YS, et al. The photopic negative response of the flash electroretinogram in multiple sclerosis. Invest Ophthalmol Vis Sci 2012;53:1315–23

47. Brigell M, Dong CJ, Rosolen S, et al. An overview of drug development with special emphasis on the role of visual electrophysiological testing. Doc Ophthalmol 2005;110:3–13
48. Johnson EC, Jia L, Cepurna WO, et al. Global changes in optic nerve head gene expression after exposure to elevated intraocular pressure in a rat glaucoma model. Invest Ophthalmol Vis Sci 2007;48:3161–77
49. Sheldon WG, Warbritton AR, Bucci TJ, et al. Glaucoma in food-restricted and ad libitum-fed DBA/2NNia mice. Lab Anim Sci 1995;45:508–18
50. Stoll G, Trapp BD, Griffin JW. Macrophage function during Wallerian degeneration of rat optic nerve: Clearance of degenerating myelin and Ia expression. J Neurosci 1989;9:2327–35
51. Moalem G, Monsonego A, Shani Y, et al. Differential T cell response in central and peripheral nerve injury: Connection with immune privilege. FASEB J 1999;13:1207–17
52. Moalem G, Leibowitz-Amit R, Yoles E, et al. Autoimmune T cells protect neurons from secondary degeneration after central nervous system axotomy. Nat Med 1999;5:49–55
53. Zimmerman LE, De Venecia G, Hamasaki DI. Pathology of the optic nerve in experimental acute glaucoma. Invest Ophthalmol 1967;6:109–25
54. Knox DL, Kerrison JB, Green WR. Histopathologic studies of ischemic optic neuropathy. Trans Am Ophthalmol Soc 2000;98:203–20
55. Shindler KS, Ventura E, Dutt M, et al. Inflammatory demyelination induces axonal injury and retinal ganglion cell apoptosis in experimental optic neuritis. Exp Eye Res 2008;87:208–13
56. Dratviman-Storobinsky O, Hasanreisoglu M, Offen D, et al. Progressive damage along the optic nerve following induction of crush injury or rodent anterior ischemic optic neuropathy in transgenic mice. Mol Vis 2008;14:2171–79
57. Domleo A, McColl G, Graham DI, et al. Quantitative evidence for continuing axonal pathology after optic nerve stretch-injury. Nuropath Appl Neurobiol 2002; 28:161
58. Maxwell WL, Kosanlavit R, McCreath BJ, et al. Freeze-fracture and cytochemical evidence for structural and functional alteration in the axolemma and myelin sheath of adult guinea pig optic nerve fibers after stretch injury. J Neurotrauma 1999;16:273–84
59. Maxwell WL. Damage to myelin and oligodendrocytes: A role in chronic outcomes following traumatic brain injury? Brain Sci 2013;3:1374–94
60. Dixon CE, Clifton GL, Lighthall JW, et al. A controlled cortical impact model of traumatic brain injury in the rat. J Neurosci Methods 1991; 39:253–62
61. Kilbourne M, Kuehn R, Tosun C, et al. Novel model of frontal impact closed head injury in the rat. J Neurotrauma 2009;26:2233–43
62. Long JB, Bentley TL, Wessner KA, et al. Blast overpressure in rats: Recreating a battlefield injury in the laboratory. J Neurotrauma 2009;26: 827–40
63. Xiong Y, Mahmood A, Chopp M. Animal models of traumatic brain injury. Nat Rev Neurosci 2013;14:128–42
64. Kumar A, Loane DJ. Neuroinflammation after traumatic brain injury: Opportunities for therapeutic intervention. Brain Behav Immun 2012;26: 1191–201
65. O'Connor WT, Smyth A, Gilchrist MD. Animal models of traumatic brain injury: A critical evaluation. Pharmacol Ther 2011;130:106–13
66. Gennarelli TA, Thibault LE, Tipperman R, et al. Axonal injury in the optic nerve: A model simulating diffuse axonal injury in the brain. J Neurosurg 1989;71:244–53
67. Povlishock JT. Traumatically induced axonal injury: Pathogenesis and pathobiological implications. Brain Pathol 1992;2:1–12
68. Povlishock JT, Christman CW. The pathobiology of traumatically induced axonal injury in animals and humans: A review of current thoughts. J Neurotrauma 1995;12:555–64
69. Buki A, Siman R, Trojanowski JQ, et al. The role of calpain-mediated spectrin proteolysis in traumatically induced axonal injury. J Neuropathol Exp Neurol 1999;58:365–75
70. Fijalkowski RJ, Stemper BD, Pintar F, et al. New rat model for diffuse brain injury using coronal plane angular acceleration. J Neurotrauma 2007;24:1387–98
71. Gennarelli TA. Mechanisms of brain injury. J Emerg Med 1993;11:5–11
72. Longhi L, Saatman KE, Fujimoto S, et al. Temporal window of vulnerability to repetitive experimental concussive brain injury. Neurosurgery 2005;56:364–74

